



Original Article

Effects of collimator on imaging performance of Yttrium-90 Bremsstrahlung photons: Monte Carlo simulation

Minho Kim ^{a, b}, Jae Keon Bae ^a, Bong Hwan Hong ^a, Kyeong Min Kim ^{a, *}, Wonho Lee ^c^a Radiation Devices Research Team, Korea Institute of Radiological and Medical Sciences, Seoul, 01812, South Korea^b Department of Bio-convergence Engineering, Korea University, Seoul, 02841, South Korea^c School of Health and Environmental Science, Korea University, Seoul, 02841, South Korea

ARTICLE INFO

Article history:

Received 24 July 2018

Received in revised form

21 October 2018

Accepted 12 November 2018

Available online 13 November 2018

Keywords:

Yttrium-90

Bremsstrahlung imaging

Collimator

Energy window

Gamma camera

ABSTRACT

Yttrium-90 is a useful therapeutic radioisotope for tumor treatment because of its high-energy-emitting beta rays. However, it has been difficult to select appropriate collimators and main energy windows for Y-90 Bremsstrahlung imaging using gamma cameras because of the broad energy spectra of Y-90. We used a Monte Carlo simulation to investigate the effects of collimator selection and energy windows on Y-90 Bremsstrahlung imaging. We considered both MELP and HE collimators. Various phantoms were employed in the simulation to determine the main energy window using primary-to-scatter ratios (PSRs). Imaging performance was evaluated using spatial resolution indices, imaging counts, scatter fractions, and contrast-to-noise ratios. Collimator choice slightly affected energy spectrum shapes and improved PSRs. The HE collimator performed better than the MELP collimator on all imaging performance indices (except for imaging count). We observed minor differences in SR and SF values for the HE collimator among the five simulated energy windows. The combination of an HE collimator and improved-PSR energy window produced the best CNR value. In conclusion, appropriate collimator selection is an important component of Bremsstrahlung Y-90 photon imaging and main energy window determination. We found HE collimators to be more appropriate for improving the imaging performance of Bremsstrahlung Y-90 photons.

© 2018 Korean Nuclear Society, Published by Elsevier Korea LLC. This is an open access article under the CC BY-NC-ND license (<http://creativecommons.org/licenses/by-nc-nd/4.0/>).

1. Introduction

Yttrium-90 (Y-90) is a radioisotope that emits high-energy electrons ($E_{\max} = 2.27$ MeV, $E_{\text{mean}} = 0.9367$ MeV) and that has been useful in targeted radionuclide therapy (TRT) approaches to treating malignant tumor diseases such as non-Hodgkin's lymphoma and unresectable liver tumors [1–4].

Y-90 is a pure electron emitter. The atom deflection and deceleration of these high-energy Y-90 electrons in tissues produces Bremsstrahlung (braking radiation) photons. These Bremsstrahlung photons are advantageous because they can be concurrently imaged using gamma cameras during treatment without surrogate radiopharmaceuticals [5,6].

Bremsstrahlung photons have continuous energy spectrum shapes with broad energy ranges. These broad ranges occur because the energy of Bremsstrahlung photons varies from 0 to the

maximum energy (2.28 MeV) of the electrons. Photon with energy values higher than 600 keV cannot be used in imaging and are not appropriate for nuclear medicine imaging using gamma cameras with collimators dedicated to conventional radioisotopes such as Tc-99m, I-123, and even I-131.

In nuclear medicine image acquisition, the energy window is the photon energy range used in imaging. In certain types of indirect conversion using scintillators (such as nuclear medicine imaging gamma cameras), photons emitted from radioisotopes are detected using main energy windows whose widths vary slightly because of the limits of the electronic circuits of detectors. It is, therefore, necessary to set the measurement range for photons in a manner such that it is centered around the main peak energy, i.e., starting from energy lower than the main peak energy and extending to energy higher than the main peak energy. This results in the main energy windows being contaminated with scattered higher energy photons.

There are two prerequisites for acquiring nuclear medicine images using a gamma camera: 1) the selection of an appropriate collimator and 2) the determination of the main energy window. A

* Corresponding author.

E-mail address: kmmkim@krams.re.kr (K.M. Kim).

collimator limits the photon angle of incidence of gamma camera system scintillator. This facilitates the rejection of scattered photons and enhances image quality. The collimator should be selected based on both the purpose of the imaging and the energy of the radioisotope emission photons that will be used in imaging. However, because of the continuous shape of the Y-90 energy spectrum (in contrast with conventional radioisotopes that have a main energy spectrum emission peak), It is difficult to determine the appropriate energy window for image acquisition and to select a collimator suitable for continuous emission energy (which can range from low energy to high energy).

Numerous studies on Bremsstrahlung gamma images have been performed in the areas of quantification, scatter and attenuation correction, and image reconstruction [7–10]. Most previous studies have focused on finding and setting the optimal energy window for gamma imaging. However, these studies have each provided different energy windows and collimators [11–14].

In this study, we evaluated Y-90 Bremsstrahlung image performance by using a Monte Carlo simulation to select an imaging window and collimator. This was done to identify a universal condition for the combination of energy windows and collimators for the better acquisition of Bremsstrahlung imaging.

2. Experiment

2.1. Set-up of Monte Carlo simulation

We performed a Monte Carlo simulation of a gamma camera using the Geant4 Application for Tomographic Emissions, v7.0 (GATE) package based on Geant4 (v4.9.6 p04) [15]. We simulated a commercial clinical SPECT camera (SYMBIA-T2, Siemens) with high-energy (HE) and medium energy low penetration (MELP) collimators (Table 1). The ME collimator is used for the imaging of gamma photons with energy values ranged from 150 keV to 400 keV, and the HE energy collimator is used for the imaging of gamma photons with energy values higher than 400 keV [16]. A SYMBIA camera has a 53.3×37.7 cm² field-of-view (FOV) and an NaI scintillator with a 0.9525 cm depth. We used information provided by the vendor to design both collimators (Table 1).

We transformed the ASCII list-type simulation output data into a planar image having a 128×128 matrix using Matlab software (R2012b).

We used the beta-spectrum information provided by the radiation dose assessment resource (RADAR, www.dose-info-radar.com) to generate the Y-90 Bremsstrahlung radiation (Fig. 1(a)) [17].

2.2. Design of phantoms

To confirm the characteristics of the simulated Bremsstrahlung spectrum, we designed a point source located in a water sphere phantom. The radii of the point source and water sphere phantom were 0.1 mm and 11 mm, respectively. The activity of the point source was 37.0 MBq. We determined that the radius of the water sphere phantom (11 mm) was equal to the maximum range in water of the beta-rays emitted from Y-90 [18]. Therefore, we

assumed that this water sphere phantom point source was equivalent to a point source for other, conventional gamma ray sources in air. To evaluate changes in the Bremsstrahlung spectrum with scattering material, four additional water sphere phantoms were generated with radii of 3, 5, 10, and 20 cm.

A 3-D voxelized human phantom, KTMAN-2 (Korean Traditional MAN-2), was implemented in the simulation to evaluate the characteristics of Y-90 Bremsstrahlung radiation with respect to the complex scattering media of the human body. KTMAN-2 is composed of $300 \times 150 \times 344$ voxels of 48 anatomical regions. The size of each voxel is $2.0 \times 2.0 \times 5.0$ mm³ [19–21]. We assumed hepatic tumor treatment conditions using radioembolization with a Y-90 microsphere. A Y-90 source of 29.859 GBq was integrated into the liver region, and the dose-distribution actor was used to identify the location of the correct Y-90 source (Fig. 1(b)). The dose-distribution actor is a specific output in the GATE simulation tools that collects the dose information during simulation.

A cylindrical phantom including six small circular rods was designed for use in calculating the contrast-to-noise ratio (CNR) (Fig. 2). All regions of the phantom were filled with water. The radii of the large circular phantom and small circles were set to 10 cm and 1 cm, respectively. The height of the cylindrical phantom was 20 cm. We assigned the six rods with activities of 18.5, 37, 74, 148, 296, and 592 MBq, respectively. The background region radioactivity has the same specific activity as the 18.5 MBq region.

2.3. Image acquisition and data analysis

All simulation data for the Bremsstrahlung spectrum was obtained in the range from 50 keV to 500 keV, which are the lower and upper limits provided by the Symbia-T2 gamma camera. The simulation time was set to 10 s.

The simulated Y-90 Bremsstrahlung spectrum was divided into two parts: a primary photon component without scattering, and a scattered component. Using the primary-to-scatter ratio, we selected an energy window that can improve image performance and applied it to further data analysis.

To evaluate image performance, we estimated the indices of spatial resolution (FWHM), scatter fractions (SF), CNRs, and image counts for both the HE and MELP collimators.

During spatial resolution estimations, point spread profiles of Gaussian model shapes were obtained from the five planar images of point sources in water sphere phantoms with varying radii. Linear interpolation and Gaussian model fitting were applied to the profile during the estimation of spatial resolution. The scatter component was estimated using scatter information included in the simulation data, and the SF was calculated by dividing the scatter component by the total components of primary and scatter counts.

$$SF = \text{scatter} / (\text{primary} + \text{scatter}) \quad (1)$$

To estimate CNR values, a circular ROI with a 10 mm radius was placed on the six rods. A region having the same specific activity as the large-cylinder phantom was set to the background area. The CNR was calculated as follows:

$$CNR = \left| \left(\frac{C - C_B}{\sigma_{BG}} \right) \right| \quad (2)$$

where C is the mean count for the ROI of the rod, C_B is the average count for the ROI of the background, and σ_{BG} is the standard deviation within the background ROI.

Table 1
Specification of collimators used in MC simulation.

	HE	MELP
Hole shape	Hexagon	Hexagon
Hole diameter (mm)	4.00	2.94
Septa thickness (mm)	2.00	1.14
Collimator length (mm)	59.70	24.05
Collimator resolution (mm)	13.20	10.80

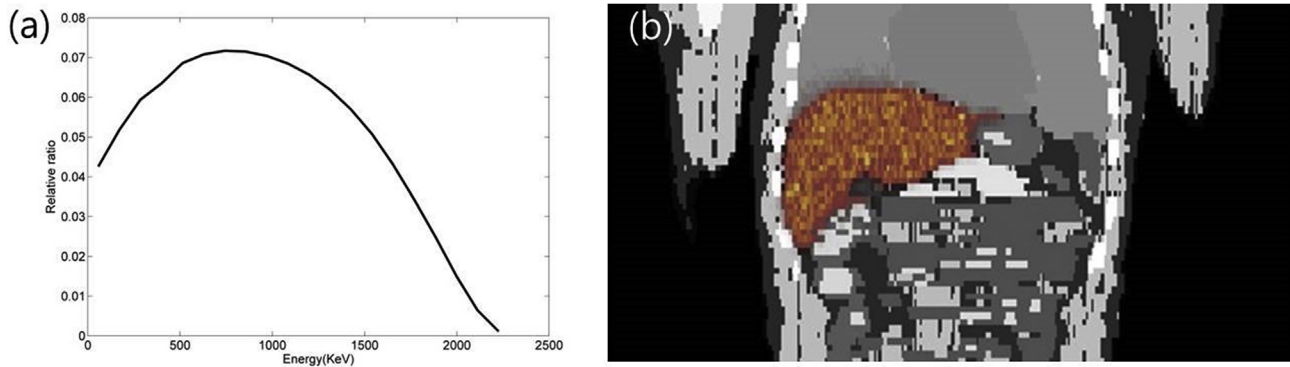


Fig. 1. (a) Beta spectrum of realized Y-90 electron source, (b) Coronal view of source location (hot-metal scale) of Y-90 by GATE actor output on KTMAN phantom (gray-scale).

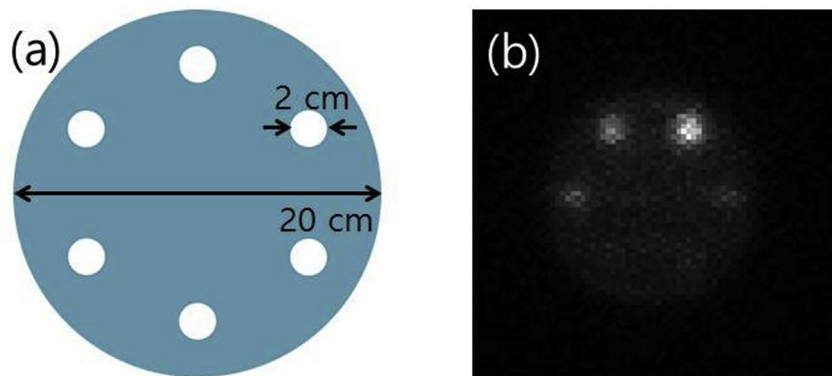


Fig. 2. (a) Transverse view of cylindrical phantom used in CNR calculations, (b) Simulated image of the cylindrical phantom.

3. Results and Discussion

3.1. Adequacy of Monte-Carlo simulation

The count histograms (i.e. energy spectra) of Bremsstrahlung Y-90 photons under various conditions could be successfully acquired and characterized. We obtained images for point sources and uptake distributions in the liver region of the voxelized human phantom; these images showed the correct locations of Y-90

sources in the phantoms (Fig. 3). From these simulation results, we confirmed that the MC simulation used in this study was adequate for use in generating Y-90 Bremsstrahlung radiation.

3.2. Characterization of energy spectrum of Bremsstrahlung photon

We observed a continuous shape for the histogram of total Bremsstrahlung photons with energy, for the phantom cases, within a wide range (50 keV–500 keV). The lower the energy, the

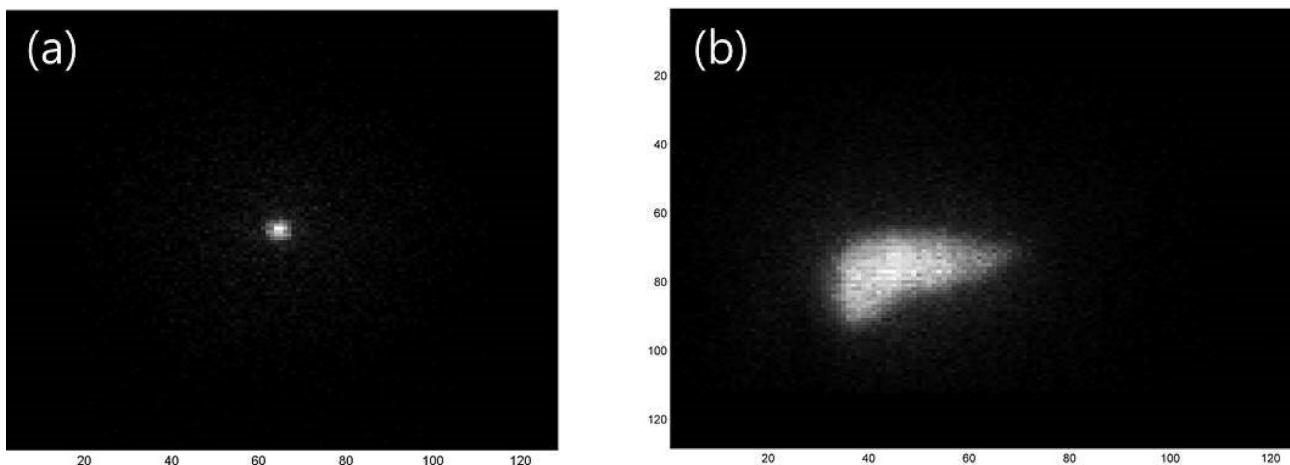


Fig. 3. Planar images obtained by Monte-Carlo simulation: (a) Y-90 point source in water-filled sphere phantom with radius of 20 cm with MELP collimator and (b) coronal view of Y-90 sources distributed in liver region of KTMAN-2 phantom.

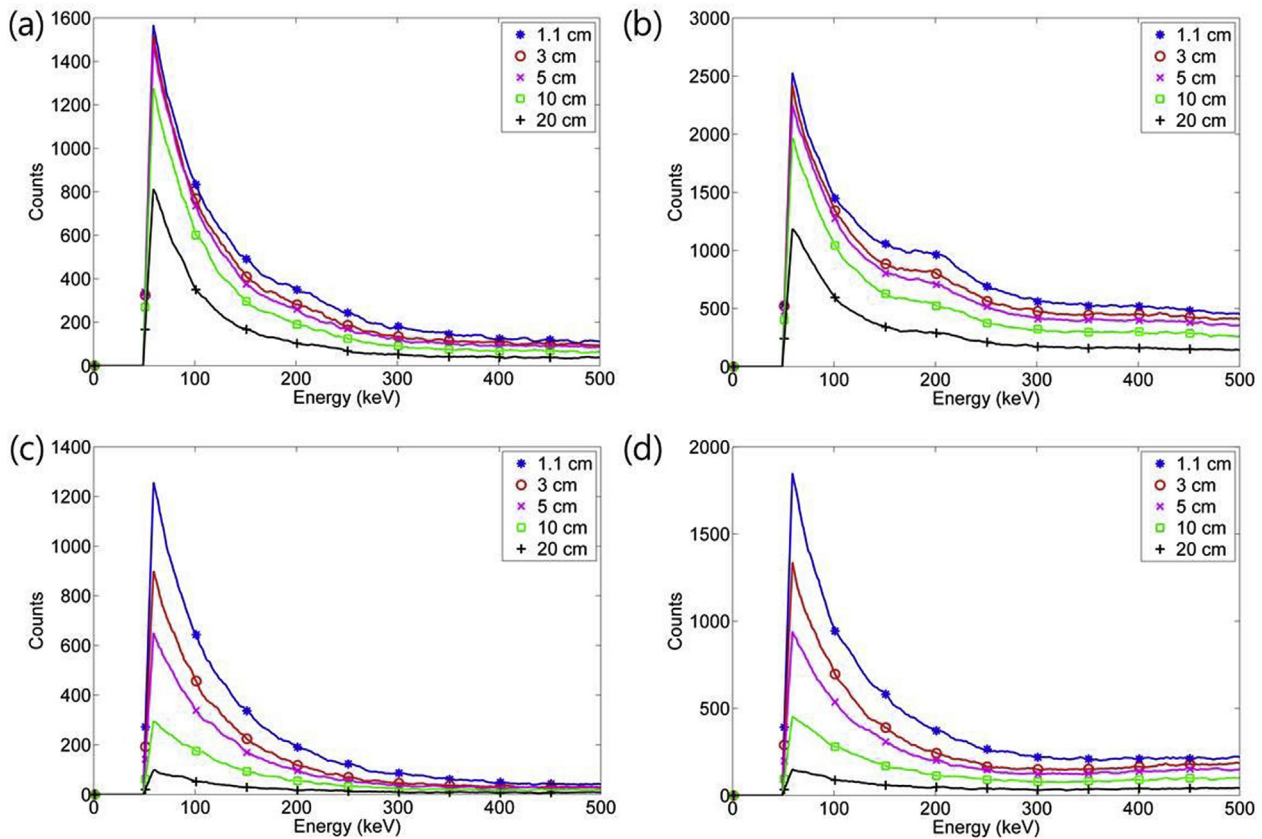


Fig. 4. Histogram of Bremsstrahlung photons with energy ranges from 50 keV to 500 keV. Histogram of total count with (a) HE collimator and (b) MELP collimator. Histogram of primary Bremsstrahlung photon with (c) HE collimator and (d) MELP collimator.

more photons were detected (Fig. 4. (a), (b)). More counts were detected by the MELP collimator than the HE collimator. However, for MELP, the higher-energy photon component increased, somewhat changing the shape of the count histogram between HE and MELP collimators. Additionally, more primary photons were detected in the low-energy range (Fig. 4. (c), (d)). When only primary photons were used for comparisons, the histograms for both collimators had similar shapes. Additionally, fewer differences were observed in the detected counts for the collimators (relative to the total counts), even with an increased number of photons in the high-energy range.

To identify the energy windows that improve imaging performance, we created histograms of the primary-to-scatter ratios (PSRs) for all phantoms for both collimators. The PSR histograms for both collimators showed higher values in the lower-energy area (similar to the histograms of total counts and primary counts). However, as the scattering material increased, PSRs decreased and exhibited more plateau-like shapes in a 10 cm radius (Fig. 5. (a), (c)).

The PSR histograms of the KTMAN phantom were very similar to those of the 10 cm radius sphere phantom. We expected the volume of the cylindrical phantom used in the simulation to be similar to the abdomen part of a human. The PSR histogram revealed energy range differences showing highest PSR for both collimators. The PSRs were highest in energy ranges of 137–184 keV for the HE collimator and 120–166 keV for the MELP collimator (Fig. 5. (b), (d)). Both histograms had PSR inflection points at approximately 200 keV. Therefore, we defined three energy windows to further evaluate image performance using three metrics: spatial resolution,

SF, and image count. We refer to additional energy windows from previous studies, as follows (Table 2).

3.3. Comparison of image performance

In images from the HE collimator, FWHM deteriorated as the amount of scatter material increased. No significant differences in FWHM were observed among the five applied energy window conditions (max 0.98 mm for a radius of 1.1 cm). Under the conditions of window 3, which had the widest energy window, FWHM deteriorated the most rapidly.

The SF also increased with the growth of water sphere phantom radii. The FWHM and SF increased more rapidly under window 3 conditions. Although the SF values were slightly dependent on the width of the energy window for sphere phantom radii smaller than 10 cm, the SF values became almost same regardless of the energy window conditions.

These results means that during the acquisition of Bremsstrahlung Y-90 photons, both FWHM and SF are affected by the amount of scatter material. The photons were slightly dependent on the setting conditions of the energy window, but this dependency was not significant.

The imaging count was dependent on the width of the energy window. In particular, both the window 3 and window 4 conditions resulted in larger counts than others, because of the wider widths and characteristics of the Y-90 Bremsstrahlung energy spectrum photons, which had large numbers of low-energy photons. CNR is the index used to evaluate the differentiation power in an image.

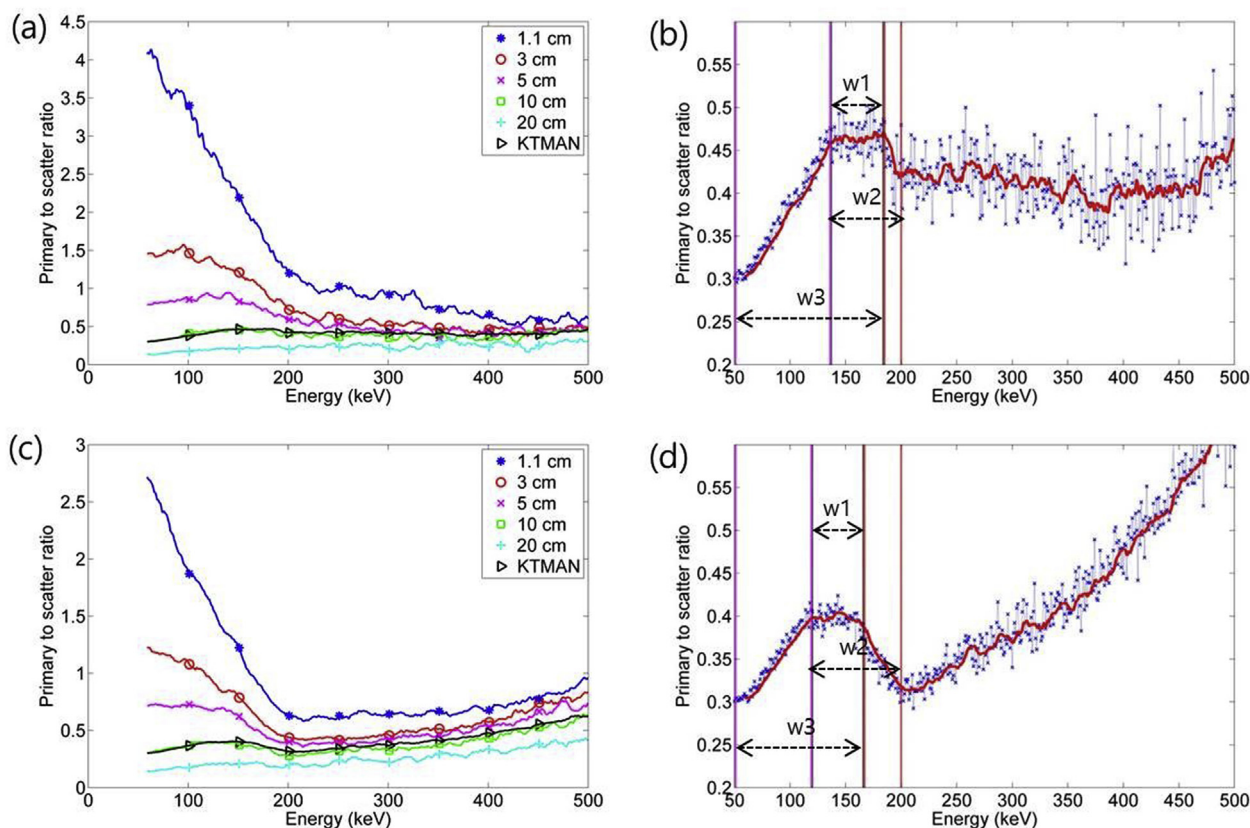


Fig. 5. (a) PSR (HE), (b) PSR in KTMAN condition (HE), (c) PSR (MELP), (d) PSR in KTMAN condition (MELP).

Table 2

Energy windows used in the evaluation of imaging performance.

Energy Windows	HE collimator (Width)	MELP collimator (Width)
Window 1	137–184 keV (47 keV)	120–166 keV (46 keV)
Window 2	137–200 keV (63 keV)	120–200 keV (80 keV)
Window 3	50–184 keV (134 keV)	50–166 keV (116 keV)
Window 4	100–160 keV (Ref. [11]) (60 keV)	60–400 keV (Ref. [13]) (340 keV)
Window 5	105–195 keV (Ref. [7]) (90 keV)	90–150 keV (Ref. [17]) (60 keV)

We observed the best CNR values for window 1, corresponding to an energy range exhibiting high PSR values. Additionally, simply expanding the energy range to both lower and higher ranges has no benefits with respect to imaging, except for increased counts (Fig. 6).

With respect to the MELP collimator results, all image performance indices were similar, but were inferior to those for the HE collimator. For an 11 mm radius sphere phantom, the value of FWHM was 19.20 ± 0.31 mm, which was larger than that of HE collimator (14.90 ± 0.41 mm of FWHM). The change in spatial resolution with the scatter material was not dependent on the energy window conditions. For the 10 cm radius sphere phantom, the FWHM was higher for windows 3 and 4, because these energy window conditions had wider ranges of energy width (and therefore more unexpected photons, which affect PSR deterioration).

The SF results and imaging counts were approximately the same as those for the HE collimator. However, the value of the imaging count was higher, because of the large numbers of photons penetrating the collimator septa.

We observed the best CNR values for window 1, which produced results similar to those for the HE collimator. However, the values were much lower and the differences with other windows were

smaller. This seems to have been caused by increased background noise due to large penetrating photons (Fig. 7).

4. Conclusion

In this study, we used a Monte Carlo simulation to assess the imaging characteristics of Y-90 Bremsstrahlung photons. In the Monte Carlo simulation, we applied a commercial SPECT camera model, with collimators used in clinical practice, and were able to obtain the energy spectra of Bremsstrahlung photons and Y-90 images under various acquisition conditions.

Among the indices used to compare imaging performance, PSR was the most useful for determining the optimal window suitable for improving Y-90 image acquisition. Other indices were not sensitive to collimator design, because of the huge amounts of high-energy Y-90 photons.

According to our PSR histogram results, the energy spectrum of the KTMAN phantom was very similar to that of the 10 cm radius phantom. For each collimator, the various energy window conditions determined from the KTMAN phantom results were used to evaluate the characteristics of imaging performance with respect to human imaging. We were able to identify the combination of

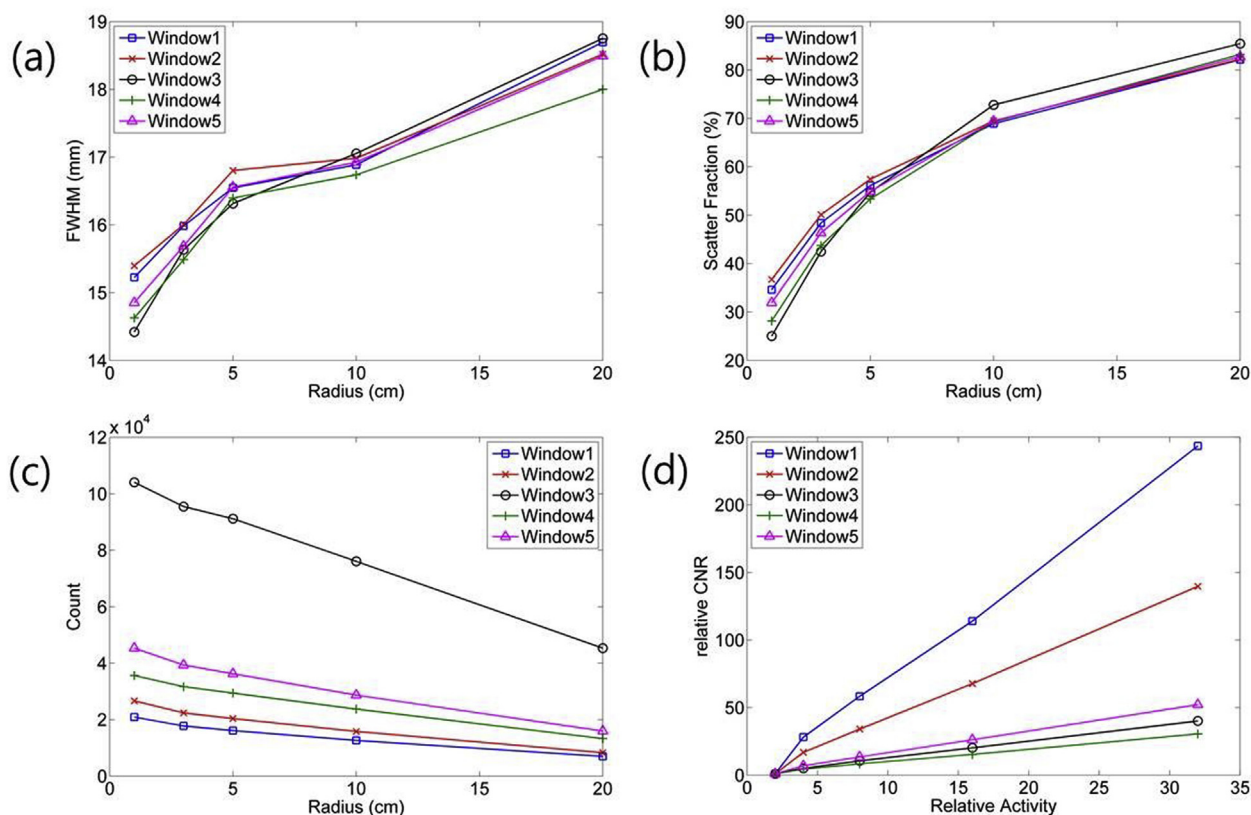


Fig. 6. Comparison of imaging performance for different energy windows using HE collimator. (a) FWHM, (b) SF, (c) imaging count, and (d) relative CNR.

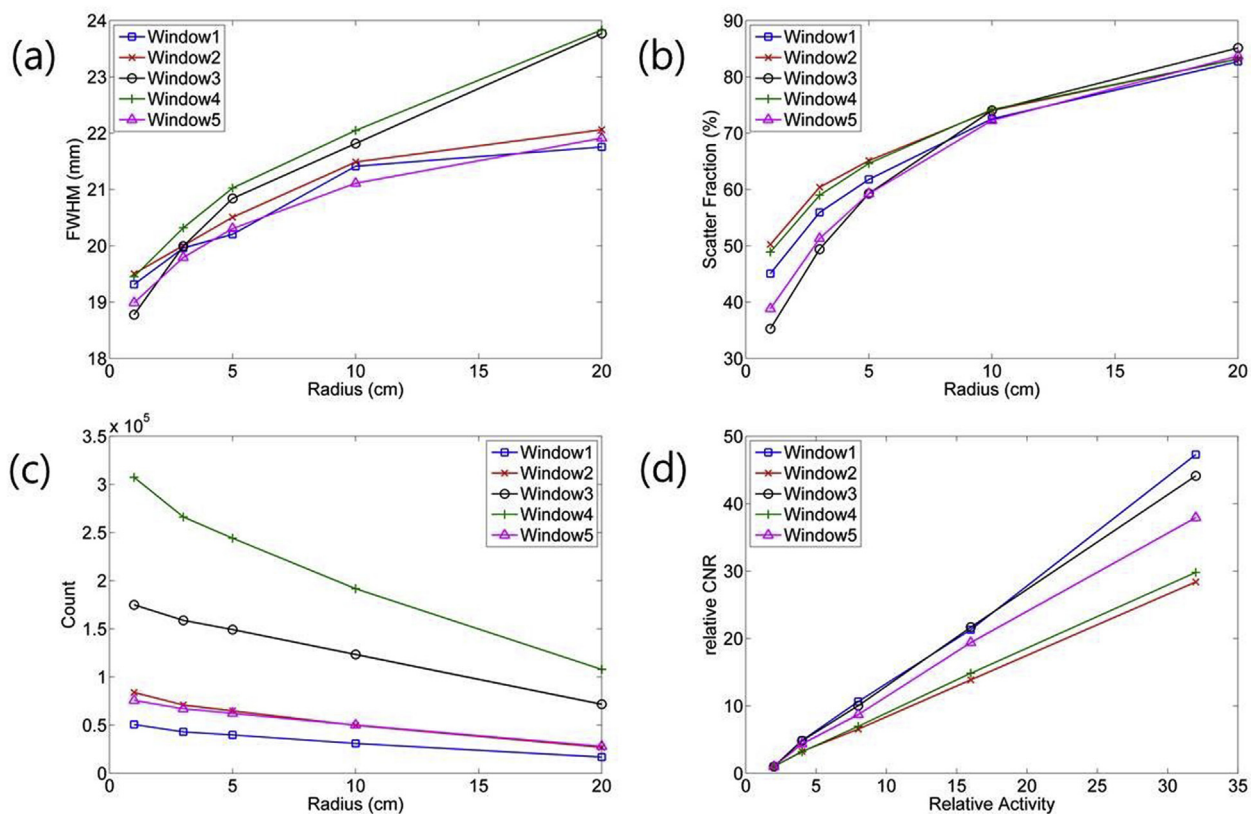


Fig. 7. Comparison of imaging performance for different energy windows using MELP collimator. (a) FWHM, (b) SF, (c) imaging count, and (d) relative CNR.

energy window and collimator that was most suitable for improving Y-90 photon imaging in humans.

In imaging using Y-90 Bremsstrahlung photon, if we consider imaging sensitivity and energy spectra with no photo peaks, MELP might be considered for use in imaging. However, the use of a MELP collimator would not improve imaging performance, because there is more non-primary photons associated with the MELP collimator (due to the large amounts of high-energy photons penetrating the collimator septa, which degrade image quality). Therefore, the HE collimator was more useful. A HE collimator with window 1 conditions could provide the best imaging performance with improved FWHM (29.57%) and CNR (492.52%) values relative to window 1 with the MELP collimator.

Considering the huge amount of radioactivity administered to patients in nuclear medicine therapy (compared to diagnostic gamma imaging), the lower imaging count rates are not a critical index to consider when choosing acquisition conditions.

Many types of gamma cameras and collimators are used in clinical practice. Therefore, various of energy window settings must be considered for improving Y-90 photon imaging. However, PSR could be a key index useful in determining the collimator and energy window, and a combination of an HE collimator and an energy window range showing higher PSR values should be desirable for acquiring images with Y-90 Bremsstrahlung photons.

This study was based on Monte Carlo simulation and the results were obtained from the simulation experiments employing a clinical SPECT camera and 3-D human phantom. The simulated images and energy spectra were enough to anticipate the characteristics of physical experimental data using Y-90. Although the energy spectrum could change slightly in the clinical approach due to the patient body and image acquisition protocol, the method presented in this paper may contribute toward obtaining better Bremsstrahlung images in the clinical approach.

Acknowledgements

This study was supported by a grant of the Korea Institute of Radiological and Medical Sciences (KIRAMS), funded by Ministry of Science and ICT (MSIT), Republic of Korea (No. 50532-2018).

References

- [1] A. Otte, R. Herrmann, A. Heppeler, M. Beche, E. Jermann, P. Powell, H.R. Maecke, J. Muller, Yttrium-90 DOTATOC: first clinical results, *Eur. J. Nucl. Med.* 26 (1999) 1439–1447.
- [2] T.E. Witzig, L.I. Gordeon, F. Cabanillas, M.S. Czuczman, C. Emmanouilides, R. Joyce, B.L. Pohlman, N.L. Bartlett, G.A. Wiseman, N. Padre, A.J. Grillo-Lopez, P. Multani, C.A. White, Randomized controlled trial of yttrium-90 –labeled ibritumomab tiuxetan radioimmunotherapy versus rituximab immunotherapy for patients with relapsed or refractory low-grade, follicular, or transformed B-cell non-hodgkin's lymphoma, *J. Clin. Oncol.* 20 (2002) 2453–2463.
- [3] F. Morschhauser, J. Radford, A. Van Hoof, U. Vitolo, P. Soubeyran, H. Tilly, P.C. Huijgens, A. Kolstad, F. d'Amore, M.G. Diaz, M. Petrini, C. Sebban, P.L. Zinzani, M.H.J. van Oers, W. van Putten, A. Bischof-Delaloye, A. Rohatiner, G. Salles, J. Kuhlmann, A. Hagenbeek, Phase III trial of consolidation therapy with yttrium-90–ibritumomab tiuxetan compared with no additional therapy after first remission in advanced follicular lymphoma, *J. Clin. Oncol.* 26 (2008) 5156–5164.
- [4] P. Flamen, B. Vanderlinden, P. Delatte, G. Ghanem, L. Ayme, M.V.D. Eynde, A. Hendisz, Multimodality imaging can predict the metabolic response of unresectable colorectal liver metastases to radioembolization therapy with Yttrium-90 labeled resin microspheres, *Phys. Med. Biol.* 53 (2008) 6591–6603.
- [5] L.P. Clarke, S.J. Cullom, R. Shaw, C. Reece, B.C. Penney, M.A. King, M. Silbiger, Bremsstrahlung imaging using the gamma camera: factors affecting attenuation, *J. Nucl. Med.* 33 (1992) 161–166.
- [6] D. Minarik, K. Sjogreen Gleisner, O. Linden, K. Wingardh, J. Tennvall, S. Strand, M. Ljungberg, ⁹⁰Y bremsstrahlung imaging for absorbed-dose assessment in high dose radioimmunotherapy, *J. Nucl. Med.* 51 (2010) 1974–1978.
- [7] D. Minarik, M. Ljungberg, P. Segars, K. Sjogreen Gleisner, Evaluation of quantitative planar ⁹⁰Y bremsstrahlung whole body imaging, *Phys. Med. Biol.* 54 (2009) 5873–5883.
- [8] X. Rong, Y. Du, M. Ljungberg, E. Rault, S. Vandenberghe, E.C. Frey, Development and evaluation of an improved quantitative ⁹⁰Y bremsstrahlung SPECT method, *Med. Phys.* 59 (2012) 2346–2357.
- [9] S. Shen, G.L. DeNardo, A. Yuan, D.A. DeNardo, S.J. DeNardo, Planar gamma camera imaging and quantitation of yttrium-90 bremsstrahlung, *J. Nucl. Med.* 35 (1994) 1381–1389.
- [10] M. Elschot, M.G.E.G. Lam, M.A.A.J. van den Bosch, M.A. Viergever, H.W.A.M. de Jong, Quantitative Monte Carlo-based ⁹⁰Y SPECT reconstruction, *J. Nucl. Med.* 54 (2013) 1557–1563.
- [11] X. Rong, Y. Du, E.C. Frey, A method for energy window optimization for quantitative tasks that includes the effects of model-mismatch on bias: application to Y-90 bremsstrahlung SPECT imaging, *Phys. Med. Biol.* 57 (2012) 3711–3725.
- [12] S. Lee, Y. Lee, Feasibility of gamma camera system with CdWO₄ detector for quantitation of yttrium-90 bremsstrahlung imaging: Monte Carlo simulation study, *Optic* 127 (2016) 11807–11815.
- [13] H.R. Roshan, B. Mahmoudian, E. Gharepapagh, A. Azarm, J.P. Islamian, Collimator and energy window optimization for ⁹⁰Y bremsstrahlung SPECT imaging: a SIMIND Monte Carlo study, *Appl. Radiat. Isot.* 108 (2016) 124–128.
- [14] X. Rong, E.C. Frey, A collimator optimization method for quantitative imaging: application to Y-90 bremsstrahlung SPECT, *Med. Phys.* 40 (2013) 1–9, 082504.
- [15] S. Jan, G. Santin, D. Strul, S. Staelens, K. Assié, D. Autret, S. Avner, R. Barbier, M. Bardiès, P.M. Bloomfield, D. Brasse, V. Breton, P. Bruyndonckx, I. Buvat, A.F. Chatzioannou, Y. Choi, Y.H. Chung, C. Comtat, D. Donnarieix, L. Ferrer, S.J. Glick, C.J. Groiselle, D. Guez, P.-F. Honore, S. Kerhoas-Cavata, A.S. Kirov, V. Kohli, M. Koole, M. Krieguer, D.J. van der Laan, F. Lamare, G. Largeron, C. Lartizien, D. Lazzaro, M.C. Maas, L. Maigne, F. Mayet, F. Melot, C. Merheb, E. Pennacchio, J. Perez, U. Pietrzyk, F.R. Rannou, M. Rey, D.R. Schaart, C.R. Schmidlein, L. Simon, T.Y. Song, J.-M. Vieira, D. Visvikis, R. Van de Walle, E. Wieers, C. Morel, GATE: a simulation toolkit for PET and SPECT, *Phys. Med. Biol.* 49 (2004) 4543–4561.
- [16] S.R. Cherry, J.A. Sorenson, M.E. Phelps, The gamma camera performance characteristics. *Physics in Nuclear Medicine*, Saunders, Philadelphia, 2012, pp. 220–225.
- [17] K.F. Eckerman, R.J. Westfall, J.C. Ryman, M. Cristy, Availability of nuclear decay data in electronic form, including beta spectra not previously published, *Health Phys.* 67 (1994) 338–345.
- [18] S.M. Rhymer, J.A. Parker, M.R. Palmer, Detection of ⁹⁰Y extravasation by bremsstrahlung imaging for patients undergoing ⁹⁰Y-ibritumomab tiuxetan therapy, *J. Nucl. Med. Technol.* 38 (2010) 195–198.
- [19] C. Lee, C. Lee, S.H. Park, J.K. Lee, Development of the two Korean adult tomographic computational phantoms for organ dosimetry, *Med. Phys.* 33 (2006) 380–390.
- [20] C. Lee, S. Park, J.K. Lee, Specific absorbed fraction for Korean adult voxel phantom from internal photon source, *Radiat. Prot. Dosimetry.* 123 (2007) 360–368.
- [21] S.H. Park, J.K. Lee, C. Lee, Dose conversion coefficients calculated using tomographic phantom, KTMAN-2 for x-ray examination of cardiac catheterisation, *Radiat. Protect. Dosim.* 128 (2007) 351–358.